Magnetically Assisted Self-Assembly of Sperm Cell Microrobot Swarms

A thesis presented for the degree of
Bachelor of Science

Clara Ostendarp
Engineering Technology – Biomedical Engineering

UNIVERSITY OF TWENTE.

SURGICAL ROBOTICS LABORATORY
WWW.SURGICALROBOTICSLAB.NL

Examination Committee:
Chair: Prof. Dr. S. Misra Supervisor: Dr. I. S. M. Khalil
External committee member: Dr. F. R. Halfwerk,
Report Number: BE-900
November 2022

Table of Contents

1 Abstract **ii**

2 Table of Symbols **ii**

3 Introduction **1**

4 Ironsperm swarm formation **1**

5 Methods **4**
5.1 Individual Ironsperm 5
5.2 Groups of Ironsperms 6
5.3 Parameters and Ranges 7

6 Results **8**
6.1 Individual Ironsperm 8
6.2 Groups of Ironsperm 10

7 Discussion **12**
7.1 Approximation as singular ellipsoids 12
7.2 Variant coating distribution forms 13
7.3 Collision mechanic 13
7.4 Adhesive force 13
7.5 Fluid dynamics 13
7.6 Conclusion 13

8 Acknowledgements **14**

1 Abstract

Microrobots that form controllable swarms are currently in the center of attention of microrobot technology research. The many advantages of swarms — detectability using imaging systems and durability in disruptive environments, among others — are of interest in the research of the biohybrid, magnetically actuated, self-propelling Ironsperm. This paper proposes a model for the mechanics of swarm formation of Ironsperms. It predicts their velocities, collision behavior, and swarm movement at low Reynolds numbers with varying applied magnetic field flux densities, applied magnetic field rotation frequencies, and viscosities of the medium in which the microrobots are suspended. The simulated, singular, ellipsoidal Ironsperm will always rotate to align its major axis with the rotating field. Multiple Ironsperms will rotate to align with the field and translate towards each other until they collide, at which point they will rotate as a unit.

2 Table of Symbols

Table 1: Table of Symbols and Units

Symbol	Explanation	Unit
f	Rotational frequency of the rotating magnetic field	Hz
η	Dynamic viscosity of the medium	Pa·s
μ_0	Magnetic permeability of vacuum	N/A^2
$\mathbf{B}$	External field flux density	T
r_i	Long radius of the ith ellipsoid	m
a_i	Short radius of the ith ellipsoid	m
V_i	Volume of the ith ellipsoid	m^3
$\mathbf{T}_m$	magnetic torque	Nm
$\mathbf{F}_m$	magnetic force	N
$\mathbf{T}_d$	drag torque	Nm
$\mathbf{F}_d$	drag force	N
$\mathbf{M}$	magnetization	A/m
$\mathbf{m}$	magnetic dipole moment	Am^2

3 Introduction

Self-propelling, remote controlled microrobots offer a modern opportunity for the treatment of internal afflictions such as cancer and arteriosclerosis. Minimally invasive surgery requires a high level of proficiency from the medical staff [1]. Enteral drug administration bears a variety of risks like lacking bioavailability, irritation of the gastrointestinal tract, and the first-pass-effect [2]. Parenteral administration of drugs can involve complications like embolisms, side effects in other organs, and even neurotoxicity [3]. Those unwanted effects could be lessened or avoided if self-propelling, remote controlled microrobots were used instead of conventional surgery or systemic drug administration. They can target specific locations that we were previously not able to reach without dispersing the drug through other organs [4, 5]. Drug delivering microrobots use natural pathways such as blood vessels or the lymphatic system to reach the site where they release a loaded drug. Those robots have to meet several design requirements to be viable to be used in the human body [6]. They have to be able to load a drug but be small enough to move through arterioles or even capillaries. They must react to external stimuli and be detectable by some imaging system, ideally without the use of radiation to reduce the invasiveness.

In recent years, the focus of medical microrobots has shifted toward swarming microrobots. A swarm is a collective of up to thousands of individual robots that behave as a coordinated unit. It requires an external energy source like a magnetic field, electric field, or a chemical gradient to affect and steer multiple robots at the same time. By externally changing the properties of the energy source, it is possible to achieve reconfigurable and variable 3D shapes like vortices and chains [7]. Being able to control the size and shape of a swarm enables microrobot movement that an unorganized swarm cannot achieve. A swarm is more difficult to disrupt, making it more durable in fast flowing fluids, and surface rolling can be applied as a mode of transportation through vessels [8]. Additionally, swarms can be detected and followed using non-invasive technology such as ultrasound. This results in easier steering and real-time feedback, allowing algorithms to automate the control of a swarm. Since each individual microrobot has a small loading capacity for a drug, control over the size of a swarm provides control over the total drug load delivered to a target site as well. The actuation of a swarm by a magnetic field provides the additional benefit that a swarm has a better responsiveness to the field than an individual microrobot, such that microrobots with weak magnetization properties can still be used [9]. The mechanics of swarm-like accumulation under influence of magnetic fields have been analyzed and understood for colloidal, round microrobots [7] and paramagnetic nanoparticles [10]. While accumulating behaviour has been observed in more complexly shaped microrobots [11], the underlying mechanics are individual to the properties of the used robots and their specific actuation method. Also, most models analyse the mechanics of swarm formation in two dimensions. A general three dimensional model has not been established yet. Yang et al. [12] provide deeper insight into the usefulness of microrobot swarms while Yu et al. [13] show that magnetically actuated, reconfigurable microrobot swarms can be controlled using the external parameters of the applied magnetic field.

4 Ironsperm swarm formation

One delivery microrobot is Ironsperm. Ironsperm is biohybrid, remote controlled, and self-propelling. An Ironsperm consists of a bovine sperm cell coated with 100 nm long, ellipsoidal, iron oxide nanoparticles. The average measurements of the four segments of an Ironsperm — head, midpiece, principal piece,

and distal end (see figure 1) — are 8.6, 13, 40, and 7 μm in length and 4.5, 1, 0.5, and 0.5 μm in width respectively [14, 15]. In an external rotating electromagnetic field its head will rotate to align with the field, emulating the natural movement of a sperm cell. A single Ironsperm can be loaded with 4.3 ± 0.2 pg of DOX-HCl, a pharmaceutical used in the treatment of various cancers [14]. Due to this small loading capacity, successful medical treatment requires multiple Ironsperms to travel to the target site, a swarm.

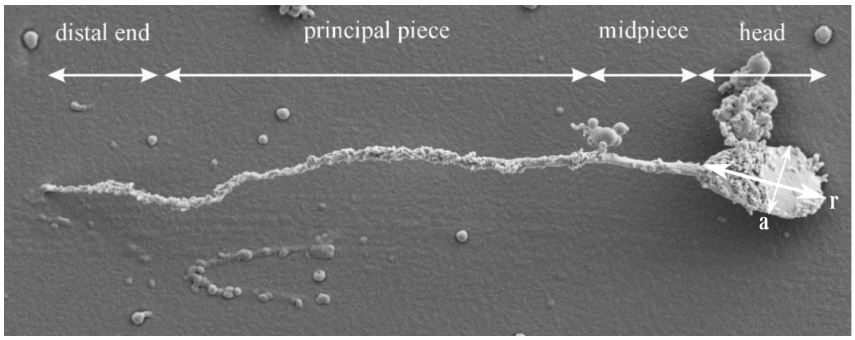

Figure 1: The modified bovine sperm cell can be divided in four distinct cellular segments: Head, midpiece, principal piece, and distal end. The smooth surface of the sperm cell is coated with iron oxide nanoparticles [14]. The ellipsoidal head can be measured along its long axis r and its short axis a.

During the coating process the nanoparticles adhere to the cellular segments. However, due to the individual differences in surface charge per cell and per section, uniform distribution of the nanoparticles cannot be guaranteed. In 93% of Ironsperms the head is coated, while the midpiece, principal piece, and distal end are coated in 44, 83, and 64% of Ironsperms respectively (see figure 2). It is beneficial if the tail sections are sparingly or not coated. If the flagellum remains flexible, its natural movement — a transverse wave along its length — to generate thrust remains intact, hence more effective propulsion. A full coating of the head allows for better response to the electromagnetic field because the head carries the most volume of the Ironsperm. There are 2^4 different way how nanoparticles can coat a sperm cell, 15 of which result in at least partially coated Ironsperms, see figure 2. These distribution forms are named in a binary way with four numerals, a 1 signifying that the cellular segment is coated and a 0 that it is not. The most desirable of those distribution forms would be form 1000 where the head is fully coated while the complete flagellum is uncoated.

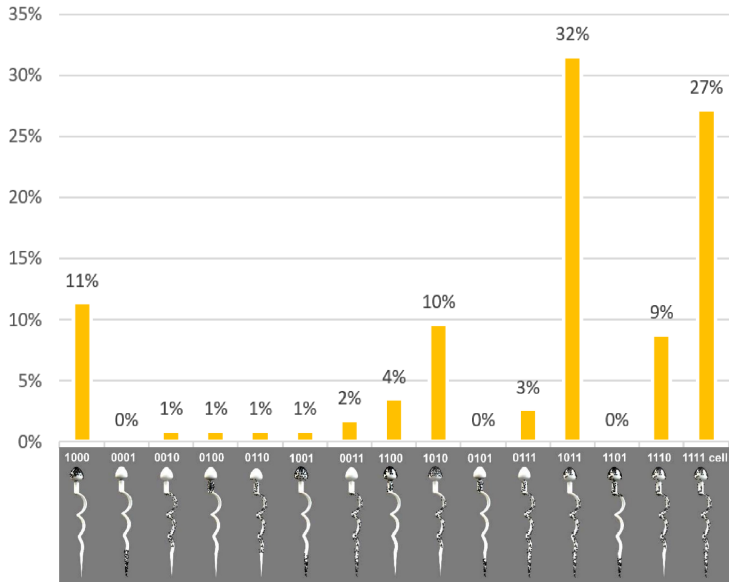

Figure 2: The coating of the sperm cells can take 15 distribution forms, not counting the null distribution because it does not result in functioning Ironsperms. Their prevalence among all coated cells is indicated as a percentage. Each four digit number is representative for its respective form, 1 meaning 'coated' and 0 meaning 'uncoated', starting with the head. Cells that have acquired no coating (form 0000) make up 2% of all trials, they are not displayed. [16]

Furthermore, the extent of how much a part of a cell is coated varies. As seen in figure 1, the head of that Ironsperm is half coated. This can occur with any part due to the proteins present in the cell's membrane [17]. Since the surface zeta potential of a sperm cell is mostly negative and the surface charge of the iron oxide nanoparticles is positive, parts of the Ironsperm that are not coated attract parts that are coated. While an Ironsperm that adheres to itself and obstructs its own flagellar movement is not functional on its own, the clustering of multiple Ironsperms presents the opportunity to use all Ironsperms: When working with swarms, all particle distribution forms can be used since the swarm's movement does not depend on flagellar movement.

Experiments have shown that Ironsperms will cluster together when immersed in a viscous fluid and actuated by a rotating magnetic field [18]. This is shown in figure 3 where a microrobot swarm is detected using ultrasound imaging and automatically tracked by software.

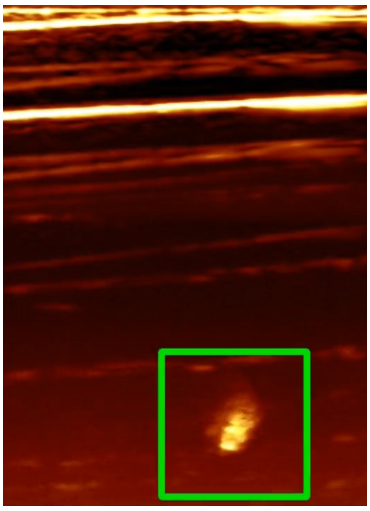

Figure 3: Detection of a microrobot swarm in an artificial blood vessel using ultrasound. At the top the vessel's surface is seen as a bright line. The swarms shows up as a bright round spot. The detection software is able to find the swarm and track it over time. Here it applies a green square that follows the swarm around as it moves. [19]

A swarm rotates as a unit at the same frequency as the applied magnetic field, see figure 4. The surrounding fluid is forced into rotation as well, thereby creating a vortex. The mechanism of how Ironsperm specifically form swarms like this is not understood yet. Their complex shape and individuality necessitate a discrete approach.

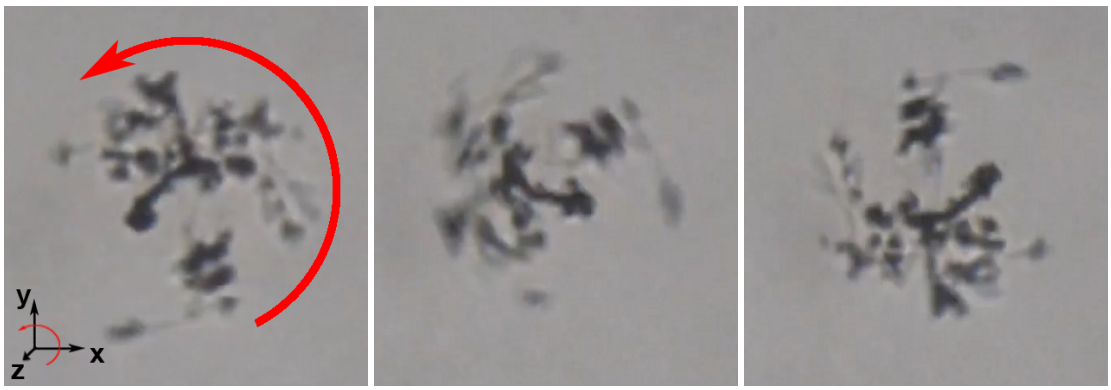

Figure 4: Three snapshots of an Ironsperm swarm over time. The applied magnetic field rotates around the z-axis, symbolized by the red curved arrow at the bottom left. The Ironsperms also rotate around the z-axis while the individual Ironsperm remain in the same constellation within the swarm.

5 Methods

To simulate the swarm formation of Ironsperms in three dimensions, each cellular segment is approximated as a prolate ellipsoid. These are attached to each other at their poles, resulting in a flexible chain of four ellipsoids. This would allow some movement in the flagellum with the attachment points functioning as joints while simulating the stiffness of Ironsperms that have coated flagellae. In the first approach, the measurements of each ellipsoid are determined by the average volume of an Ironsperm and the length of the corresponding Ironsperm segment with an adjustment for the average amount of nanoparticles on each segment, see figure 5a. In the second approach, the average length and width of each segment

determine the measurements of the ellipsoids, see figure 5b. Each ellipsoid has a random charge based on the coating distribution forms, either positive or negative. These approaches were not pursued further due to the complexity of implementing their movements in 3D over time using a MATLAB [20] script.

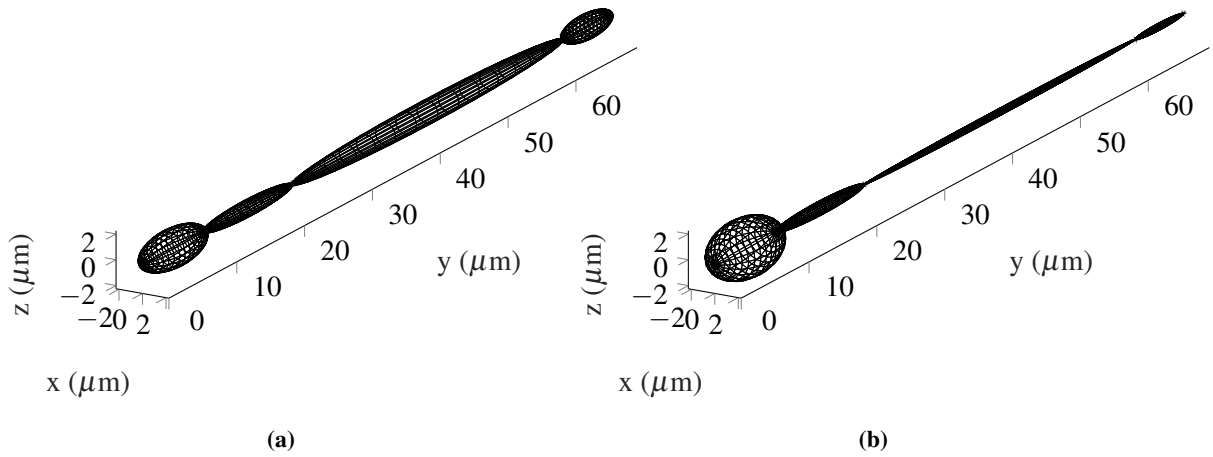

Figure 5: Two proposed 3D representations of Ironsperm. Each cellular segment is approximated as a prolate ellipsoid. In **(a)** the measurements of each ellipsoid are based on length an volume of each segment and adjusted for the average amount of nanoparticle coating. The shape and size of the ellipsoids in **(b)** are plainly based on the average length and width of each segment.

To simplify Ironsperm microrobots, the heads of the Ironsperms are approximated as ellipsoids the size of the average Ironsperm head. The segments that form the flagellum are omitted. The Ironsperm head is the most voluminous out of the four segments and therefore its magnetic moment is the highest. This simplification resulted in an in silico model that lets the ellipsoids interact with each other over time and under influence of a rotating magnetic field.

5.1 Individual Ironsperm

The head of an Ironsperm is a prolate ellipsoid. Abbott et al. [21] provide the demagnetization factors as follows:

$$\begin{aligned} n_r &= \tfrac{1}{R^2-1}\left(\tfrac{R}{2\sqrt{R^2-1}}\ln\left(\tfrac{R+\sqrt{R^2-1}}{R-\sqrt{R^2-1}}\right)-1\right) \\ n_a &= \tfrac{1-n_r}{2} \end{aligned} \tag{1}$$

with $R = r/a$ being the ratio between the long radius r of the body and the short radius a of the body. The demagnetization factors n_r and n_a relate to r and a as well. Since we deal with soft-magnetic materials, Abbott et al. [21] show that the susceptibility matrix χ is simplified to

$$\chi = \operatorname{diag}\left(\frac{1}{n_r}, \frac{1}{n_a}, \frac{1}{n_a}\right). \tag{2}$$

The magnetization $\mathbf{M}$ of an individual Ironsperm resulting from the magnetic field flux density $\mathbf{B}$ is dependent on the susceptibility matrix χ and the constant permeability of vacuum $\mu_0 = 4\pi \times 10^{-7}$ N/A^2. Both $\mathbf{M}$ and $\mathbf{B}$ must be written with respect to the ellipsoid's frame of reference, and we have

$$\mathbf{M} = \chi\left(\frac{1}{\mu_0}\mathbf{B}\right) \tag{3}$$

In this model, a body's frame of reference is calculated using inclination and azimuth. At both angles equal to zero, the ellipsoid's axis of symmetry e_1 — the "long" axis — coincides with the x-axis of the laboratory frame of reference Ψ_0, seen later in chapter Results. The rotation to the ellipsoid's frame of reference is achieved using standard coordinate transformation:

$$\mathbf{B} = \begin{bmatrix} e_{11} & e_{12} & e_{13} \\ e_{21} & e_{22} & e_{23} \\ e_{31} & e_{32} & e_{33} \end{bmatrix} \mathbf{B}_{\Psi_0} \tag{4}$$

with $\mathbf{B}_{\Psi_0}$ being the field flux density with respect to the laboratory frame of reference.

The opposing forces and torques in a system with one ellipsoid within low Reynolds numbers are limited to the magnetic force and torque, and the drag force and torque, such that

$$\begin{aligned} \mathbf{F}_m &= \quad -\mathbf{F}_d \\ \mathbf{T}_m &= \quad -\mathbf{T}_d. \end{aligned} \tag{5}$$

The magnetic force $\mathbf{F}_m$ induced by the applied field is negligible because the field can be assumed as homogeneous considering the size of the ellipsoid. Therefore, the drag force $\mathbf{F}_d$ is zero as well and we have a pure rotation. The drag torque uses the following drag coefficients

$$\begin{aligned} C_{T1} &= \quad 0 \\ C_{T2} &= \quad \tfrac{4}{3}e^3 \left(\tfrac{2-e^2}{1+e^2}\right) \left(-2e + (1+e^2)\ln\tfrac{1+e}{1-e}\right)^{-1} \\ C_{T3} &= \quad C_{T2} \end{aligned} \tag{6}$$

with $e = \sqrt{1 - a^2/r^2}$ [22]. The drag coefficient C_{T1} equals zero because the ellipsoid's geometry is not affected by rotation around e_1. Therefore, the drag torque around e_1 can be neglected. The drag torque

$$\mathbf{T}_d = 8ra^2\pi\eta\mathbf{C}_T\omega \tag{7}$$

with η being the dynamic viscosity of the medium, and the magnetic torque

$$\mathbf{T}_m = V\mathbf{M} \times \mathbf{B} \tag{8}$$

give the torques around axes e_1 (roll), e_2 (pitch), and e_3 (yaw). They are used in equation 5 to obtain the angular velocity ω and its integral θ. The angular displacement θ is then used in the pure rotation matrix

$$R = \begin{bmatrix} \cos|\theta| + \theta_x^2(1-\cos(|\theta|)) & \theta_x^2\theta_y^2(1-\cos|\theta|) - \theta_z\sin|\theta| & \theta_x^2\theta_z^2(1-\cos|\theta|) + \theta_y\sin|\theta| \\ \theta_y^2\theta_x^2(1-\cos|\theta|) + \theta_z\sin|\theta| & \cos|\theta| + \theta_y^2(1-\cos|\theta|) & \theta_y^2\theta_z^2(1-\cos|\theta|) - \theta_x\sin|\theta| \\ \theta_z^2\theta_x^2(1-\cos|\theta|) - \theta_y\sin|\theta| & \theta_z^2\theta_y^2(1-\cos|\theta|) + \theta_x\sin|\theta| & \cos|\theta| + \theta_z^2(1-\cos|\theta|) \end{bmatrix} \tag{9}$$

to calculate the next position of the ellipsoid, given by $e_{i,new} = R \cdot e_i$.

5.2 Groups of Ironsperms

When assembled in swarms, Ironsperms are subjected to interactive forces and torques in addition to the drag force and torque exerted on the individual microrobot. The interactive forces between two Ironsperms are dependent on the distance between them, in this model approximated by the distance vector **d** from center to center of two ellipsoids.

The field flux density $\mathbf{B}$ and magnetization $\mathbf{M}$ are calculated as above to obtain the induced magnetic dipole $\mathbf{m} = V\mathbf{M}$ which is used to obtain the magnetic force and torque of ellipsoid i in a swarm of n ellipsoids [8].

$$\begin{aligned}
\mathbf{F}_{m,i} = & \sum_{j=1,j\neq i}^{n} \frac{3\mu_0}{4\pi \mathbf{d}_{ji}^4} \left((\hat{\mathbf{d}}_{ji} \times \mathbf{m}_i) \times \mathbf{m}_j + (\hat{\mathbf{d}}_{ji} \times \mathbf{m}_j) \times \mathbf{m}_i - 2\hat{\mathbf{d}}_{ji}(\mathbf{m}_i \cdot \mathbf{m}_j) + 5\hat{\mathbf{d}}_{ji}(\hat{\mathbf{d}}_{ji} \times \mathbf{m}_i) \cdot (\hat{\mathbf{d}}_{ji} \times \mathbf{m}_j) \right) \\
\mathbf{T}_{m,i} = & \mathbf{m}_i \times \mathbf{B}_i + \sum_{j=1,j\neq i}^{n} \mathbf{m}_i \times \left(\frac{\mu_0}{4\pi} \frac{3\hat{\mathbf{d}}_{ji}(\hat{\mathbf{d}}_{ji} \cdot \mathbf{m}_i) - \mathbf{m}_i}{|\mathbf{d}_{ji}|^3} \right),
\end{aligned} \tag{10}$$

where $\mathbf{d}_{ji}$ is the vector from the center of ellipsoid j to ellipsoid i and $\hat{\mathbf{d}}_{ji}$ its unit vector.

On collision, the adhesive force $\mathbf{F}_a$ and contact force $\mathbf{F}_c$ will add to the equation of forces. $\mathbf{F}_c$ prevents the ellipsoids to move through each other and equals the opposite of the force in the direction of the collision site. $\mathbf{F}_a$ keeps the ellipsoids attached to each other, as has been observed in experiments, see figure 4.

$$\mathbf{F}_a = \mathrm{k}\hat{\mathbf{d}}_{ij} \tag{11}$$

The spring constant $\mathrm{k} = 4 \times 10^{-7}$ N/m is chosen such that $\mathbf{F}_a$ is in the same order of magnitude as $\mathbf{F}_m$ when collision has occurred.

The drag force

$$\mathbf{F}_d = 6r\pi\eta\mathbf{C}_F v \tag{12}$$

with coefficients

$$\begin{aligned}
C_{F1} = & \tfrac{8}{3}e^3 \left(-2e + (1+e^2)\ln\tfrac{1+e}{1-e}\right)^{-1} \\
C_{F2} = & \tfrac{16}{3}e^3 \left(2e + (3e^2-1)\ln\tfrac{1+e}{1-e}\right)^{-1} \\
C_{F3} = & C_{F2}
\end{aligned} \tag{13}$$

is then used to calculate the translational velocity v of each ellipsoid.

5.3 Parameters and Ranges

For both, individual and multiple ellipsoids, the following parameters and their influence on the model are to be investigated. These are properties of the Ironsperm movement mechanism that can be individually controlled and changed. In experiments, in vitro or in vivo, especially f and $\mathbf{B}$ are simple to change.

Table 2: Parameters and Ranges

Parameter	minimum value	maximum value
f	1 Hz	50 Hz
$\mathbf{B}$	1 mT	10 mT
η	1 mPa·s	50 mPa·s

Additionally, for pairs of ellipsoids the initial distance between their centers of mass d_{initial} is investigated. The investigation range goes from 10 μm, when the ellipsoids are already attached to each other, to 30 μm. The maximum value is chosen such that a collision can be achieved within a reasonable simulation time. While f and $\mathbf{B}$ are chosen in the ranges that can be reproduced in experiments with Ironsperms, η is chosen such that it encompasses the dynamic viscosities of water at room temperature, mammalian plasma, as well as mammalian whole blood and lymph [23, 24, 25] to be able to model Ironsperms' behavior under the circumstances of their supposed use.

6 Results

6.1 Individual Ironsperm

A singular ellipsoid starts stationary in a predetermined position. At field flux density $\mathbf{B} = 0$, it remains in its position indefinitely, since no forces or torques act on it. At $\mathbf{B} > 0$ it first rotates in the opposite direction of the field, to align its major axis with the applied rotating magnetic field (see figure 6). Afterwards, it rotates at the same ω as the field. The maximum angular velocity ω_{max} occurs while the ellipsoid rotates its major axis toward the field direction. The alignment of the ellipsoid's major axis with the field t_{align} is asymptotic. For the purpose of this paper, alignment is defined as achieved when ω is within 0.1 rad/s of the field's velocity.

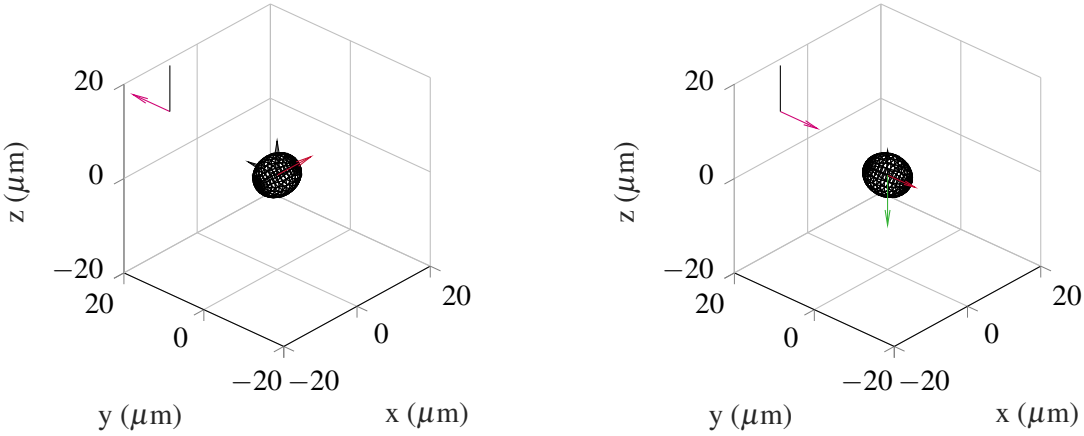

(a) Starting position

(b) End position

Figure 6: The individual ellipsoid in its starting position and after a half revolution of the applied field. In its starting position, seen on the left, its major axis (red) is not aligned with the applied magnetic field represented by the arrows on the top left. The magenta arrow signifies the direction of the applied magnetic field rotating around the axis of rotation (black). On the right, the ellipsoid is aligned with the field after the field has rotated 180°, with the green arrow being the angular velocity vector.

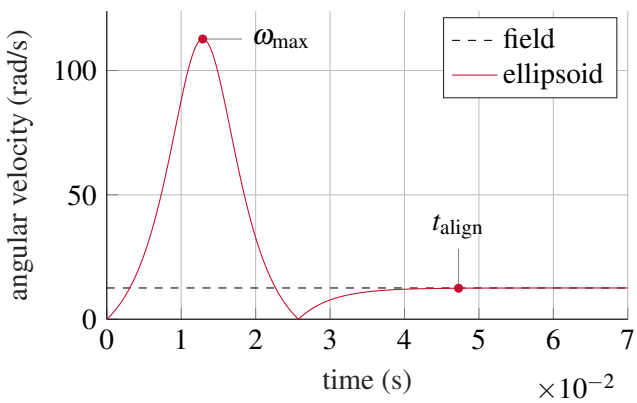

Figure 7: At a field flux density $\mathbf{B}$ of 1 mT at a rotational frequency f of 2 Hz in a medium with $\eta = 1$ mPa·s, the singular ellipsoid will align with the field after 0.047 seconds. Before, it will reach a maximum angular velocity ω_{max} of 112.7 rad/s at $t = 0.013$. The field is rotating at a velocity of 12.57 rad/s.

The relations of ω_{max}, $t_{\omega_{\text{max}}}$, and t_{align} with $\mathbf{B}$, f, and η behave as follows, as can be derived from figure 8:
The maximum angular velocity increases as the field flux density increases, such that $\omega_{\text{max}} \propto \text{m}\mathbf{B}$ with $1.19 < \text{m} < 4.00$ and $\text{m} \propto 1/\nabla\mathbf{B}$. There is no relation of ω_{max} with the frequency of the rotating field: $\omega_{\text{max}} \neg \propto f$. An increased medium viscosity η decreases ω_{max}, until ω_{max} is smaller than the field velocity, thus $\omega_{\text{max}} \propto \text{m}/\eta$ with $0.50 < \text{m} < 0.90$ and $\text{m} \propto \nabla\eta$.
The time at which ω reaches its peak is reverse proportional to the field flux density, specifically $t_{\omega_{\text{max}}} \propto \text{m}/\mathbf{B}$ with $0.35 < \text{m} < 0.90$ and $\text{m} \propto \nabla\mathbf{B}$. Though it increases as the field frequency increases: $t_{\omega_{\text{max}}} \propto \text{m}f$ with $0.81 < \text{m} < 0.98$ and $\text{m} \propto \nabla f$. The influence of η is that $t_{\omega_{\text{max}}} \propto \eta$ until a threshold is reached at which no global peak of ω is noticeable anymore. With $\mathbf{B} = 1$ mT and $f = 2$ Hz, this threshold is at $\eta = 9$ mPa·s. At higher η the ellipsoid cannot rotate at the same speed as the field and falls behind. The field continues rotating until the ellipsoid's "north pole" has an angle to the field direction > 90°. At that point, the ellipsoid will flip directions to attempt to align with the field with the "north pole" now being the "south pole".
The time of alignment of the ellipsoid with the field is proportional to the field flux density, $t_{\text{align}} \propto \mathbf{B}$. Its relation to the field frequency is parabolic, thus $t_{\text{align}} \propto$ a function of f^2, with the vertex being dependent on f as well as $\mathbf{B}$. With increasing η, t_{align} increases as well, in detail $t_{\text{align}} \propto \text{m}\eta$ with $1.22 < \text{m} < 2.05$, though m increases when $\eta < 0.4$ mPa·s and when $\eta > 0.5$ mPa·s.

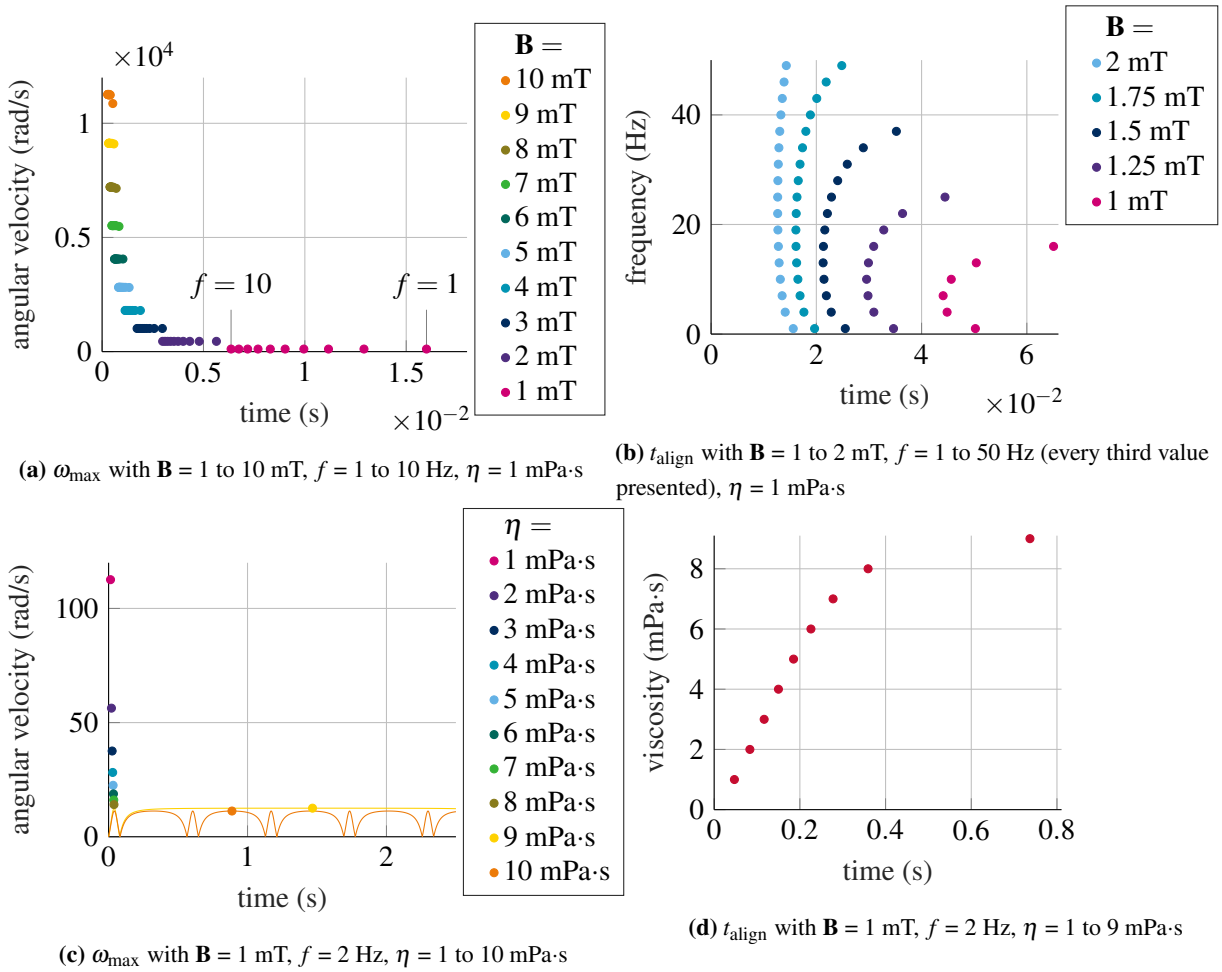

(a) ω_{max} with **B** = 1 to 10 mT, f = 1 to 10 Hz, η = 1 mPa·s

(b) t_{align} with **B** = 1 to 2 mT, f = 1 to 50 Hz (every third value presented), η = 1 mPa·s

(c) ω_{max} with **B** = 1 mT, f = 2 Hz, η = 1 to 10 mPa·s

(d) t_{align} with **B** = 1 mT, f = 2 Hz, η = 1 to 9 mPa·s

Figure 8: The changes of ω_{max} and t_{align} depending on different values of **B**, f, and η. **(a)** At increasing amplitudes, ω_{max} increases by a factor of 2 each time **B** is increased by 1 mT. The point in time when the ellipsoid reaches ω_{max} increases by a factor of 1.2 to 1.7. **(b)** The alignment of the ellipsoid with the field takes an amount of time that increases as **B** increases. The frequency f influences it in a parabolic way. **(c)** An increase of η decreases ω_{max}. At $\eta \geq 9$ mPa·s the initial spike of ω is smaller than the velocity of the rotating field, such that ω_{max} occurs when the ellipsoid has aligned with the field. At η = 10 mPa·s the ellipsoid cannot rotate fast enough to align with the field, such that asymptotic approach of the field's velocity never occurs. **(d)** An increase of η increases t_{align}.

6.2 Groups of Ironsperm

Ellipsoids influence the behavior of other ellipsoids that are in close proximity. At $\mathbf{B} > 0$ the magnetic force induced by the rotating field pulls the ellipsoids toward each other. While the ellipsoids align their major axes with the field, their centers of mass translate in a spiral on the rotation plane of the field, with the general direction being dictated by the closest ellipsoids. When the distance d between two ellipsoids understeps the threshold of 22.64 μm (for $\mathbf{B} = 1$ mT, $f = 2$ Hz, $\eta = 1$ mPa·s), v increases exponentially and the two ellipsoids collide (see figure 9b). The angular velocity ω spikes as each ellipsoid aligns its major axis with the field direction. After alignment, ω fluctuates under influence of the nearby ellipsoids. At collision, ω reaches a local maximum but subsides to fluctuate around the angular velocity of the field within less than 0.1 s.

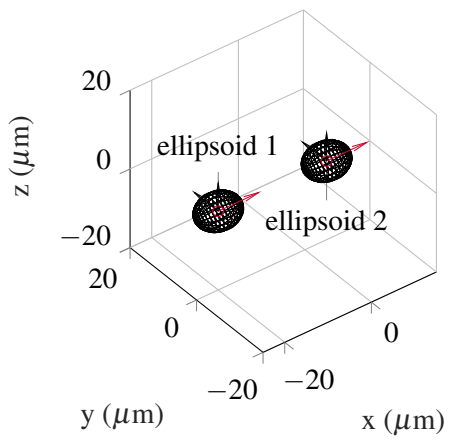

(a) Starting position

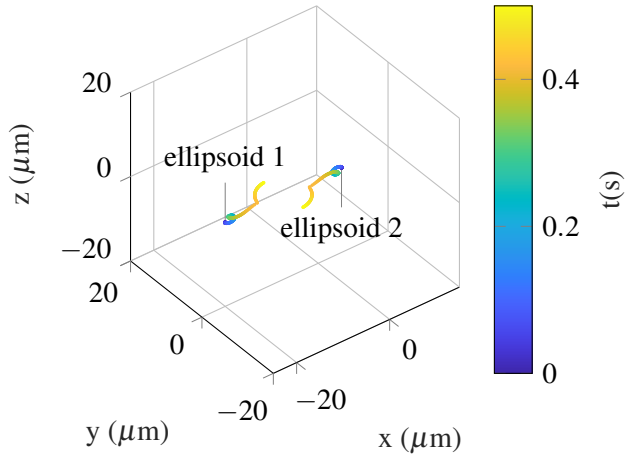

(b) Trajectories of centers of mass over one field rotation

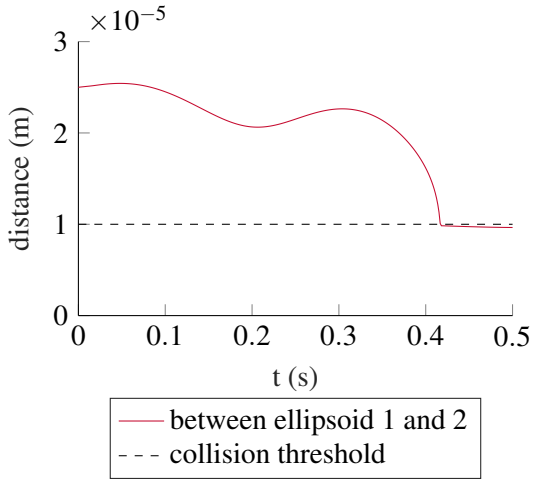

(c) distance between the centers of mass of the ellipsoids

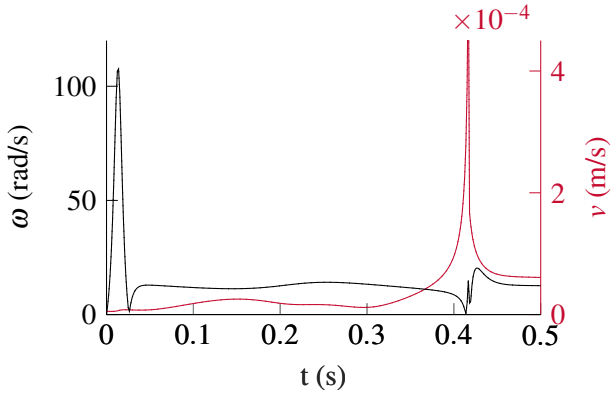

(d) translational and angular velocities of both ellipsoids

Figure 9: Two ellipsoids at a distance of 25 μm under influence of a rotating magnetic field with f = 2 Hz and **B** = 1 mT in a medium with η = 1 mPa·s will collide after 0.42 s. Afterwards, they rotate around their combined center of mass while staying attached to each other. The translational velocity v and angular velocity ω of one ellipsoid equal those of the other, hence the full overlap in **(d)**.

The influence of different **B** and f on a pair of ellipsoids can be seen in figure 10. For pairs of ellipsoids, it is of interest how long it takes until they collide. At an increasing field frequency f, the time it takes for the two ellipsoids to collide t_{coll} decreases, $t_{\text{coll}} \propto \text{m}/f$. Though t_{coll} approaches a minimum, so $\text{m} \propto 1/f$. As **B** increases above 3 mT, t_{coll} decreases, $t_{\text{coll}} \propto 1/\mathbf{B}$. At **B** < 3 mT, the ellipsoids do not move as quickly as at higher **B**. This means, the ellipsoids do not move close enough within the simulated timeframe to collide. The sudden increase of t_{coll} at **B** = 2 mT and f = 6 Hz is due to a bigger spiral that the ellipsoids both describe. It increases their distance and thus it takes longer until the ellipsoids collide. Increased initial distance d_{initial} between the ellipsoids increases t_{coll}, $t_{\text{coll}} \propto \text{m}d_{\text{initial}}$ with $\text{m} \propto d_{\text{initial}}$. At an initial distance of 10 μm, t_{coll} occurs at t = 0 since the collision threshold is set at 10 μm. The viscosity of the medium η is approximately linearly related to t_{coll}, such that $t_{\text{coll}} \propto \text{m}\eta$ with m being dependent on η and d_{initial}. There is a wave-like fluctuation in t_{coll} due to the varying amount of spirals that the ellipsoids make when approaching each other.

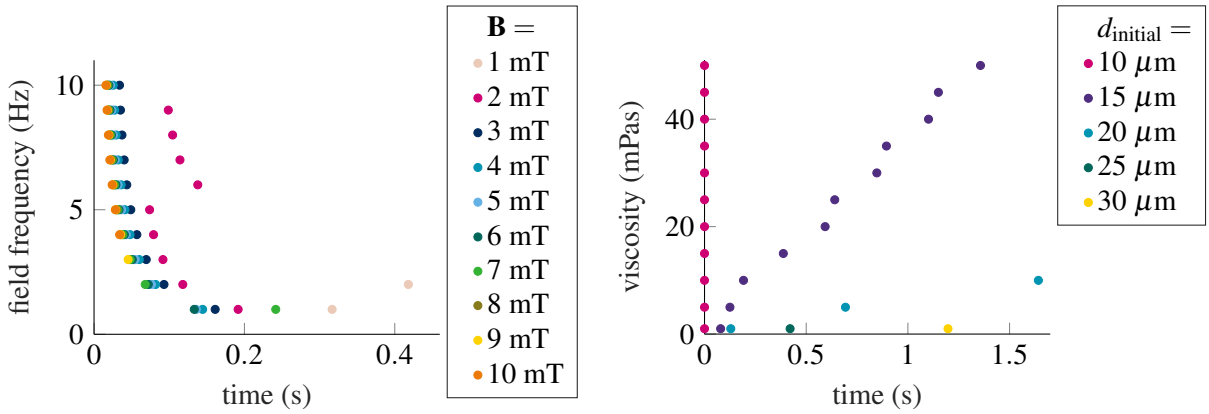

(a) η = 1 mPa·s, d_{initial} = 25 μm

(b) **B** = 1 mT, f = 2 Hz

Figure 10: The time of collision t_{coll} for two ellipsoids. **(a)** At increasing **B**, t_{coll} will decrease and asymptotically approach a minimum. That minimum is determined by f. It decreases as f increases. **(b)** At increasing η, t_{coll} increases approximately linearly. At increasing d_{initial}, t_{coll} increases.

7 Discussion

Controlling Ironsperm swarms would enable medical staff to safely deliver drugs to a target site using the natural pathways of the human body. For this to become reality, more understanding of the formation of Ironsperm swarms was required. This theoretical model shows the mechanism of how Ironsperm swarms form and thus provides a base for research into the control of their size and shape. The external field's parameters f and **B** allow for precise control of the velocities of Ironsperm. The medium viscosity η is a factor that is likely not possible to externally manipulate in in vivo situations, but it influences the behavior of Ironsperm, as shown in this model, and must therefore be accounted for when controlling a swarm in a precise manner.

The presented model is purely theoretical and based on observations made during experiments with Ironsperm that did not focus on swarm formation. It takes numerous liberties in simplifying the concept of an Ironsperm swarm. This results in reduced value of the model when focusing on details. Nevertheless, it shows the general behavior of Ironsperms in swarms and can function as a base for further research and more intricate models in the future. The following details should be considered when evaluating the accuracy of this model.

7.1 Approximation as singular ellipsoids

The approximation of Ironsperms as singular ellipsoids the size and shape of an Ironsperm head is acceptable when calculating the influence of the applied field. But in Ironsperm swarms, it is possible that their tails entangle, influencing the shape and motility of the swarms. The movement of an Ironsperm head can be described as a cone-like rotation of the major axis where the tip of the cone is close to the end where the flagellum is attached. The reason for this movement is that the flagellum creates additional drag [26]. Also, a high concentration of nanoparticles on the flagellum, e.g. a 1111 distribution, can result in a stiff flagellum that impairs the Ironsperm's movement further. The drag coefficients used here are accurate for the Ironsperm head only. The movement of the ellipsoids thus does not accurately show this cone-like rotation.

7.2 Variant coating distribution forms

The magnetic attraction of the ellipsoids in the model towards each other has no conditions, except for the necessity of the presence of a rotating magnetic field. In reality, an Ironsperm's surface charge is dependent on its mode of coating. As mentioned above, this is highly individual. Parts of an Ironsperm's head can have a positive surface charge, some negative. Hence, an Ironsperm can be attracted to only a part of another or even not at all attracted to another. In what configuration whole Ironsperms with variant distribution forms adhere to each other in a swarm is therefore unpredictable with this model.

7.3 Collision mechanic

The way collision is implemented here is flawed. The distance between ellipsoids is measured using their centers of mass and not their surfaces. Collision is registered when the distance between two centers of mass is equal to or smaller than a fixed threshold. This threshold can be visualized as a sphere around an ellipsoid with a diameter equal to the length of the ellipsoid's major axis. Hence, the threshold lies outside the actual surface of the ellipsoid except at the poles. Therefore, the model can assume that collision occurred even if two ellipsoids do not touch.

7.4 Adhesive force

The spring constant k used in the calculation of $\mathbf{F}_a$ is not based in science but obtained experimentally within the model. There is no conclusive research into the adhesive properties of Ironsperm yet. Though it has been observed that coated parts of an Ironsperm can adhere to uncoated parts of the same or another Ironsperm. Thus, the approximation of the adhesive force as a simple spring force is necessary.

7.5 Fluid dynamics

A rotating Ironsperm swarm can affect the surrounding medium such that it is set in motion. A fluid vortex created in this manner could influence the integrity of the swarm and Ironsperms in its vicinity. This is not included in the model because small swarms do not create fluid vortices big enough to enact a significant force on surrounding Ironsperm.

7.6 Conclusion

Regardless of the limitations this model has, it is capable to model the influence of the external conditions f, $\mathbf{B}$, and η on individual Ironsperm heads as well as pairs of Ironsperm heads. As a result, it also models the formation of Ironsperm swarms if any influence of the flagellae is omitted. This model presents the first step of analysing Ironsperm swarm behavior in three dimensions. To be able to model and understand a three dimensional swarm is necessary to ultimately control its shape, size, and movement through the three dimensional environment of the human body.

The next step in exploring the swarm formation of Ironsperms is to verify and adjust the presented model with experiments. Further research into the adhesive properties of Ironsperms is also needed. The model can be expanded by adding more ellipsoids to get a sense of big swarm interactions or by including flagellae. For this, the abovementioned first approach (with each segment modelled as an ellipsoid) or a model with chain-like flagellae can be implemented fully to accommodate for the drag and spacial influence of flagellae and different distribution forms.

8 Acknowledgements

The author majorly thanks their supervisor Dr. Islam Khalil for his guidance and patience. They thank their examination committee and the members of the Surgical Robotics Lab for providing feedback and data. They also thank Dr. Veronika Magdanz and Dr. Juliane Simmchen for their interest in this study as well as the data they provided. Lastly, Anneloes Dekker-Dummer deserves thanks for her guidance and insight.

References

[1] L. P. Stassen, W. A. Bemelman, and J. Meijerink, "Risks of minimally invasive surgery underestimated: a report of the dutch health care inspectorate," pp. 495–498, 2010.

[2] P. Verma, A. Thakur, K. Deshmukh, A. Jha, and S. Verma, "Routes of drug administration," *International Journal of Pharmaceutical Studies and Research*, vol. 1, no. 1, pp. 54–59, 2010.

[3] V. Schirrmacher, "From chemotherapy to biological therapy: A review of novel concepts to reduce the side effects of systemic cancer treatment," *International journal of oncology*, vol. 54, no. 2, pp. 407–419, 2019.

[4] M. Luo, Y. Feng, T. Wang, and J. Guan, "Micro-/nanorobots at work in active drug delivery," *Advanced Functional Materials*, vol. 28, no. 25, p. 1706100, 2018.

[5] K. Park, "Facing the truth about nanotechnology in drug delivery," *ACS nano*, vol. 7, no. 9, pp. 7442–7447, 2013.

[6] D. Liu, T. Wang, and Y. Lu, "Untethered microrobots for active drug delivery: From rational design to clinical settings," *Advanced Healthcare Materials*, vol. 11, no. 3, p. 2102253, 2022.

[7] H. Xie, M. Sun, X. Fan, Z. Lin, W. Chen, L. Wang, L. Dong, and Q. He, "Reconfigurable magnetic microrobot swarm: Multimode transformation, locomotion, and manipulation," *Science robotics*, vol. 4, no. 28, p. eaav8006, 2019.

[8] L. Yang and L. Zhang, "Motion control in magnetic microrobotics: From individual and multiple robots to swarms," *Annual Review of Control, Robotics, and Autonomous Systems*, vol. 4, pp. 509–534, 2021.

[9] M. Sitti and D. S. Wiersma, "Pros and cons: Magnetic versus optical microrobots," *Advanced Materials*, vol. 32, no. 20, p. 1906766, 2020.

[10] J. Yu, L. Yang, and L. Zhang, "Pattern generation and motion control of a vortex-like paramagnetic nanoparticle swarm," *The International Journal of Robotics Research*, vol. 37, no. 8, pp. 912–930, 2018.

[11] P. J. Vach, D. Walker, P. Fischer, P. Fratzl, and D. Faivre, "Pattern formation and collective effects in populations of magnetic microswimmers," *Journal of Physics D: Applied Physics*, vol. 50, no. 11, p. 11LT03, 2017.

[12] L. Yang, J. Yu, S. Yang, B. Wang, B. J. Nelson, and L. Zhang, "A survey on swarm microrobotics," *IEEE Transactions on Robotics*, 2021.

[13] J. Yu, L. Yang, X. Du, H. Chen, T. Xu, and L. Zhang, "Adaptive pattern and motion control of magnetic microrobotic swarms," *IEEE Transactions on Robotics*, 2021.

[14] V. Magdanz, I. S. Khalil, J. Simmchen, G. P. Furtado, S. Mohanty, J. Gebauer, H. Xu, A. Klingner, A. Aziz, M. Medina-Sánchez *et al.*, "Ironsperm: Sperm-templated soft magnetic microrobots," *Science advances*, vol. 6, no. 28, p. eaba5855, 2020.

[15] C. G. Gravance, R. Vishwanath, C. Pitt, D. L. Garner, and P. J. Casey, "Effects of cryopreservation on bull sperm head morphometry," *Journal of Andrology*, vol. 19, no. 6, pp. 704–709, 1998.

[16] V. Magdanz, J. Vivaldi, S. Mohanty, A. Klingner, M. Vendittelli, J. Simmchen, S. Misra, and I. S. Khalil, "Impact of segmented magnetization on the flagellar propulsion of sperm-templated microrobots," *Advanced science*, vol. 8, no. 8, p. 2004037, 2021.

[17] V. Magdanz, J. Gebauer, P. Sharan, S. Eltoukhy, D. Voigt, and J. Simmchen, "Sperm–particle interactions and their prospects for charge mapping," *Advanced Biosystems*, vol. 3, no. 9, p. 1900061, 2019.

[18] K. Middelhoek, V. Magdanz, L. Abelmann, and I. Khalil, "Drug-loaded ironsperm clusters: modeling, wireless actuation, and ultrasound imaging," *Biomedical Materials*, 2022.

[19] I. Khalil, A. Klingner, and S. Misra, *Mathematical Modeling of Swimming Soft Microrobots*, 1st ed. Academic Press, 2021, ch. 9.

[20] MATLAB, *MATLAB version 9.10.0.1613233 (R2021a)*. Natick, Massachusetts: The MathWorks Inc., 2021.

[21] J. J. Abbott, O. Ergeneman, M. P. Kummer, A. M. Hirt, and B. J. Nelson, "Modeling magnetic torque and force for controlled manipulation of soft-magnetic bodies," *IEEE Transactions on Robotics*, vol. 23, no. 6, pp. 1247–1252, 2007.

[22] I. Khalil, A. Klingner, and S. Misra, *Mathematical Modeling of Swimming Soft Microrobots*, 1st ed. Academic Press, 2021, ch. 5.

[23] U. Windberger, A. Bartholovitsch, R. Plasenzotti, K. Korak, and G. Heinze, "Whole blood viscosity, plasma viscosity and erythrocyte aggregation in nine mammalian species: reference values and comparison of data," *Experimental physiology*, vol. 88, no. 3, pp. 431–440, 2003.

[24] G. Lowe and J. Barbenel, "Plasma and blood viscosity," in *Clinical blood rheology*. CRC Press, 2019, pp. 11–44.

[25] J. B. Dixon, S. T. Greiner, A. A. Gashev, G. L. Cote, J. E. Moore Jr, and D. C. Zawieja, "Lymph flow, shear stress, and lymphocyte velocity in rat mesenteric prenodal lymphatics," *Microcirculation*, vol. 13, no. 7, pp. 597–610, 2006.

[26] I. Khalil, A. Klingner, and S. Misra, *Mathematical Modeling of Swimming Soft Microrobots*, 1st ed. Academic Press, 2021, ch. 4.